This paper appears in IEEE Transactions on Biomedical Engineering
https://ieeexplore.ieee.org/document/10173580
LOGO DOI: 10.1109/TBME.2023.3290472

Improved Configurations for 3D Acoustoelectric Tomography with a Minimal Number of Electrodes

Ben Keeshan, Andy Adler, and Carlos Rossa

***Abstract*— Objective: Acoustoelectric tomography (AET) is a hybrid imaging technique combining ultrasound and electrical impedance tomography (EIT). It exploits the acoustoelectric effect (AAE): an US wave propagating through the medium induces a local change in conductivity, depending on the acoustoelectric properties of the medium. Typically, AET image reconstruction is limited to 2D and most cases employ a large number of surface electrodes. Methods: This paper investigates the detectability of contrasts in AET. We characterize the AEE signal as a function of the medium conductivity and electrode placement, using a novel 3D analytical model of the AET forward problem. The proposed model is compared to a finite element method simulation. Results: In a cylindrical geometry with an inclusion contrast of 5 times the background and two pairs of electrodes, the maximum, minimum, and mean suppression of the AEE signal are 68.5%, 3.12%, and 49.0%, respectively, over a random scan of electrode positions. The proposed model is compared to a finite element method simulation and the minimum mesh sizes required successfully model the signal is estimated. Conclusion: We show that the coupling of AAE and EIT leads to a suppressed signal and the magnitude of the reduction is a function of geometry of the medium, contrast and electrode locations. Significance: This model can aid in the reconstruction of AET images involving a minimum number of electrodes to determine the optimal electrode placement.**

***Index Terms*— Electrical Impedance Tomography, Acoustoelectric Tomography, Acoustoeletric effect**

I. Introduction

ELECTRICAL impedance tomography (EIT) [1] is an inexpensive, portable, and non-invasive imaging technique with many applications in medical imaging; the dominant clinical application is the monitoring of lung function ([2], [3]) but EIT also boast successes in monitoring hemodynamics and related heart function ([4], [5]), in addition to promise with regards to imaging blood flow within the brain ([6], [7]) and the detection of cancer ([8], [9]). EIT involves reconstructing interior conductivity distributions from voltage and current measurements on the boundary of a body, and the EIT inverse problem is inherently ill-posed and thus suffers from poor resolution and instabilities. To address these limitations a hybrid imaging technique known as acoustoelectric tomography (AET) has been developed [10], [11]. AET relies on the acoustoelectric effect (AEE) [12], [13], [14] which is driven by local conductivity changes produced by a ultrasound (US) pressure wave as it moves through a body. The time-dependent AEE perturbations lead to changes in the EIT measurements, from which the conductivity can then be reconstructed with high resolution. Unfortunately, the AEE signal is extremely small effect and can be quite difficult to measure.

Fig. 1 panels (a) and (b) illustrates the AET sensitivity, which is proportional to σJ_{EIT}, where J_{EIT} is the EIT sensitivity for conductivity changes induced by the US pulse. As the conductivity of the anomaly increases (by Δ above the background, σ), the Electric field $\vec{E}$ decreases, by a factor of $(1+\frac{\Delta}{2\sigma})$. In this scenario, $J_{\mathrm{EIT}} \propto \sigma\|\vec{E}\|^2$ and showing the AET sensitivity is reduced to $(\frac{\sigma+\Delta}{\sigma+\frac{1}{2}\Delta})^2$, in this example. This reduction of the AET sensitivity has not previously been reported, and is a function of the anomaly conductivity and geometry and the EIT stimulation and measurement configuration. Panels (c) and (d) in Fig. 1, show the effect of an US perturbation within a cylinder as it travels through the homogeneous background and an inclusion. The effect is quite small and is magnified in the bottom panel of Fig. 1 (c) and (d). See supplemental material for a video of this effect.

The vast majority of the AET literature focuses on the last step of the AET process, i.e., reconstructing the conductivity from an assumed known power density [11], [15], [16], [17], [18]. Recently, more comprehensive methods to solve the AET problem have tackled the initial step of solving for the power density. In [19] the authors used a difference EIT measurement and singular value decomposition (SVD) based reconstruction to find the boundary potential and an initial conductivity reconstruction. In [20] a 2-dimensional EIT forward problem is solved involving Neumann boundary conditions (BCs) and a regularized least squares approach to reconstruct the power density. The conductivity is then reconstructed from the power density by solving a regularized

The authors are with the Department of Systems and Computer Engineering, Carleton University, Ottawa, ON Canada. Email: benkeeshan@cmail.carleton.ca; adler@sce.carleton.ca; rossa@sce.carleton.ca.

We acknowledge the support of the Natural Sciences and Engineering Research Council of Canada (NSERC), the Canadian Institutes of Health Research (CIHR), and the Social Sciences and Humanities Research Council of Canada (SSHRC), [funding reference number NFRFE-2018-01986].

Cette recherche a eté financée par le Conseil de recherches en sciences naturelles et en génie du Canada (CRSNG), par les Instituts de recherche en sante du Canada (IRSC), et par le Conseil de recherches en sciences humaines du Canada (CRSH), [numéro de référence NFRFE-2018-01986]

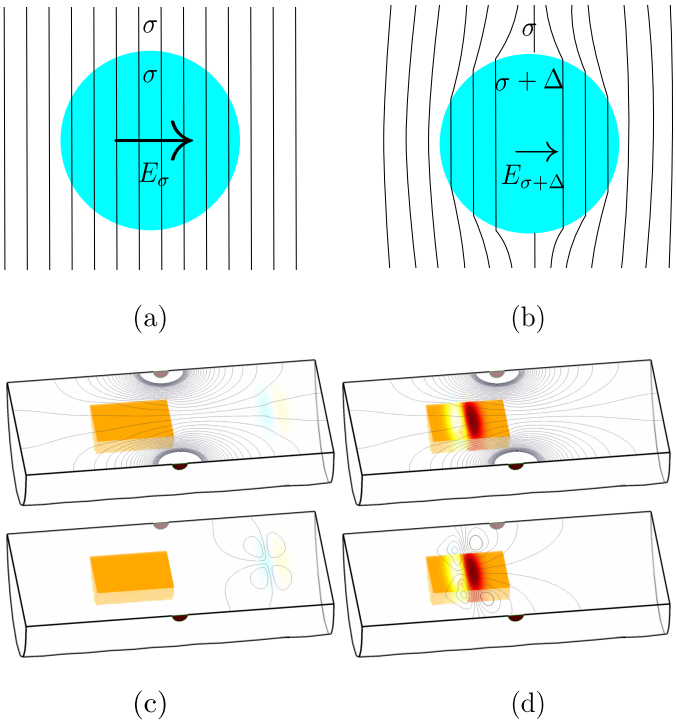

Fig. 1. Top: Illustration of AET sensitivity: equipotential lines around a cylindrical conductive anomaly (left $\boldsymbol{\sigma}$, right $\boldsymbol{\sigma + \Delta}$) with measurement and current drive is on parallel plates far away. Electric field $\vec{\boldsymbol{E}_{\sigma+\Delta}}$ is reduced from $\vec{\boldsymbol{E}_{\sigma}}$ by a factor of $(\mathbf{1} + \frac{\boldsymbol{\Delta}}{\mathbf{2}\boldsymbol{\sigma}})$. This decreased electric field means the AET signal, the US-induced change in $\boldsymbol{\sigma}$, is also reduced. Bottom: Conductivity changes are larger when the pulse is in a conductive region (right). Current is applied between red electrodes and electric equipotentials are shown. The lower figure shows the change in potential due to the US pulse.

functional. In [21] the authors developed an approach that incorporated the uncertainty in the propagation of the acoustic pressure wave. For a review see [22].

In most of the literature, the AET inverse problem is implemented using a large number of surface electrodes, and it is mostly limited to a 2D plane. While this allows for a reasonable reconstruction of the electrical potential along the boundary, it substantially limits the applications of AET. A current open challenge in AET is to solve the inverse problem using a minimal number of surface electrodes in a volumetric medium. A robust understanding of the forward problem provides an insight into the physical interplay between the EIT and AEE, can guide the design of experimental system, determine the optimal position of electrodes and the ultrasound wave forms that maximize the strength of the measured signal.

As illustrated, the coupling betweeen the AEE and EIT signals reduces the signal compared to a naive expectation. It is therefore important to understand the interplay between the EIT sensitivity and the AEE when considering the feasibility of an AET system. In order to accomplish this, one must consider the 3D case; as the current flow cannot be confined to a 2D plane. The difficulties introduced by this competition are minimized by a system with a large number of surface electrodes.

There are several clinical applications of an AET system with a minimum number of measurement electrodes. An example of a potential application would be an *in- vivo* imaging system that involves dual-purpose electrodes/biopsy needles. The feasibility of such a potentially powerful system rests upon three fundamental questions: (1) Will the competition between the EIT sensitivity and AEE suppress the extremely small AEE signal to the point where it cannot be measured? (2) If the signal is large enough to be detected, has this competition washed away enough of the local conductivity dependence as to render any attempt at reconstruction futile? And (3) is the computational power needed for an realistic simulation of the 3D forward problem small enough to be practical?

Furthermore, any practical AET system faces two very serious challenges; the signal-to-noise ratio (SNR) will have to be very low and in practice the US wave speed, an essential input of a forward model, is an experimental unknown. A minimal 3D experimental setup is thus a very useful test of the practicality of AET systems. If it is impossible to achieve a sufficiently low SNR that allows for a reconstruction of a simplified setup it will almost certainly be impossible to reconstruct conductivities for a clinical application.

In order to answer these questions, this paper introduces a new 3D model for the AET forward problem for a system with a minimal number of electrodes in a simple cylindrical geometry. This allows us to examine the problem analytically in terms of a simple eigenfunction expansion. This model allows us to analyze the EIT sensitivity's conductivity dependence and determine the interplay of geometric considerations and changing inclusion contrasts on current flow. This model also allows for the fast simulation of the effect of changing electrode placement on the AET waveform, and an estimation of the optimal electrode placement. i.e. a configuration that maximizes the amplitude of the AET signal. As the model also allows for a computationally inexpensive simulation of the forward problem, it can be used to estimate the numerical footprint required to implement a realistic simulation of the 3D AET forward problem, which incorporates the complete electrode model (CEM) [23], [24], [25] in a framework well-suited to solving the 3D inverse problem. As the model describes a minimal experimental setups, it also allows one to place an upper bound on the SNR needed for a practical realization of AET.

This paper's contributions are as follows:

1) We show for the first time the dependency of the AEE signal and the EIT sensitivity, which has fundamental implications for the feasibility of practical AET systems;
2) We introduce a convenient parameterization of the AET forward problem, which allows for easy integration of the 3D AET problem with preexisting EIT packages; and
3) We introduce an accurate and computationally efficient analytical model of the EIT forward problem for a simple geometry.

II. Acoustoeletric Signal Suppression

The starting point of AET is the EIT forward problem, namely to find the potential within some closed subspace, Ω,

of R^n ($n = 2, 3$) with a smooth boundary, $\partial\Omega$, and no interior current sources. The potential inside Ω is found by solving the generalized Laplace equation:

$$\nabla \cdot \sigma(\boldsymbol{x})\nabla\Phi(\boldsymbol{x}) = 0, \tag{1}$$

where $\sigma(x)$ is the conductivity distribution within Ω and $\Phi(x)$ is the quasi-static electric potential, subject to some boundary conditions (BCs). In the complete electrode model (CEM) [23], [24] the mixed BCs are (for N electrodes):

$$\begin{aligned} \int_{E_i} j dA &= I_i \\ j &= 0 \text{ on } \Gamma' \\ \Phi + z_i\sigma\vec{\nabla}\Phi \cdot \hat{\rho} &= V_i \text{ on } \Gamma, \end{aligned} \tag{2}$$

where E_i, z_i, σ, V_i, and I_i are the surface, impedance, conductivity, voltage, and current of the i^{th} electrode respectively, $\Gamma = \bigcup_i E_i$, $\Gamma' = \partial\Omega - \Gamma$, and the surface current density, j, is given by:

$$j = \sigma(\boldsymbol{x})\nabla\Phi(\boldsymbol{x}) \cdot \hat{n}, \tag{3}$$

where $\hat{n}$ is the outward unit normal vector of the surface and j satisfies $\int_\partial \Omega j = 0$.

In general, when the medium is perturbed with an ultrasound pulse, the change to the local conductivity can be modelled by the simple linear relation [26]:

$$\sigma_p(\boldsymbol{x}, t) = \sigma(\boldsymbol{x}) + \delta\sigma(\boldsymbol{x}, t) = \sigma(\boldsymbol{x}) + kp(\boldsymbol{x}, t)\sigma(\boldsymbol{x}). \tag{4}$$

Here, $k = \mathcal{O}(10^{-8}$,$10^{-9})$ is a coupling constant in Pa^{-1}, while $p(\boldsymbol{x}, t)$ is the ultrasound pressure at position $\boldsymbol{x}$ and time t. The perturbed potential obeys its own version of (1) with conductivity σ_p and potential u_p. If the non-perturbed boundary conditions are maintained, the result is a perturbation to the power needed to maintain the boundary condition. If the US pulse passes through the medium while an EIT measurement is being performed it will also introduce a small time dependent perturbation into the EIT measurement. To first order, the dissipating power is given by [11]:

$$P_d(t) = -k\int_\Omega p(\boldsymbol{x}, t)\sigma|\nabla u|^2 dV = k\int_\Omega p(\boldsymbol{x}, t)M(\sigma)dV, \tag{5}$$

where $M(\sigma)$ is known as the power density and $dV = dx^3$. Equation (5) is a Fredholm equation of the first kind and the AET inverse problem is to reconstruct the conductivity σ given a known $p(\boldsymbol{x}, t)$ and some measurements of $M(\sigma)$. Similarly, for a unit current input, let resulting perturbation in an EIT voltage measurement given some drive and measurement pattern is [1]:

$$\delta V_{inj,m} = -\int_\Omega \delta\sigma\nabla u_{inj}\nabla u_m dV = -\int_\Omega \delta\sigma E_{inj} \cdot E_m dV, \tag{6}$$

where $_{inj}$ is the potential corresponding to the injection electrodes while u_m is the potential produced if the measurement electrodes are stimulated with a unit current.

If the conductivity is discretized into N elements (e.g., voxels or tetrahedral elements), $\delta\sigma$ becomes a constant over each voxel and (6) defines the EIT Jacobian or the sensitivity matrix:

$$J^{EIT}_{dm,k} = \frac{\partial V_{d,m}}{\partial\sigma_k} = -\int_{\Omega_k} \nabla u(I_d)\nabla u(I_m)dV. \tag{7}$$

Equations (6) and (7) allow one to parameterize the AET forward problem in terms of the traditional EIT forward problem. i.e.,

$$\delta V_i^{AEE}(t) = J^{EIT}\boldsymbol{\delta\sigma} = kJ^{EIT}_{il}p(t)_l\sigma_l, \tag{8}$$

where is $\delta V_i^{AEE}(t)$ the difference between the measured voltage of the i^{th} EIT measurement as a function of time and the unperturbed measurement. Using this parameterization, the AET inverse problem consists of two steps. The first, a linear inverse problem, is to use the measured voltages and an a priori US model to reconstruct the power density, $M_{ij} = J^{EIT}_{ij}\sigma_j$ while the second is to a nonlinear inversion of M.

While a cursory examination of (8) suggests a strong proportionality between the local conductivity perturbed by the US and the AEE signal, this will compete with the Jacobian's implicit dependence on σ. In fact, a naive analysis suggests that the AEE signal has a rather troublesome functional dependence on σ. For a given voxel, the current density is $j = \sigma E$, where E is the electric field. Assuming the current density is locally constant, $E \approx \frac{j}{\sigma}$, gives:

$$J^{EIT} = \sigma|E|^2 \approx \frac{|j|^2}{\sigma}. \tag{9}$$

Plugging (9) into (8) with the (unrealistic and first order) assumption of constant current flow gives:

$$\delta V_i \approx kp(t)_j\frac{1}{\sigma_j}\sigma_j. \tag{10}$$

which results in an exact cancellation of the dependence on local conductivity. While this first-order assumption is obviously overly pessimistic, it does imply that the AEE signal is suppressed relative to the naive expectation. If this cancellation is strong enough, the signal's dependence on conductivity will be dominated by its dependence on the geometry of the body, complicating the solution to the AET inverse problem.

III. 3D Analytical Model of AET

The AET signal is found by solving (6) for a given US waveform. The US waveform can be modelled as a travelling wave packet normally distributed about the beam axis. It will be sufficient for our purposes to use the following simplified model:

$$\begin{aligned} p(\rho, \phi, z, t) =& P_0 e^{-\left(\frac{\rho\cos(\phi)-x_0}{w_1}\right)^2} e^{-\left(\frac{\rho\sin(\phi)-y_0}{w_1}\right)^2} \\ & \left(e^{-\left(\frac{z-ct}{2w_2}\right)^2}\sin\left[2\pi f(z-ct)\right]\right), \end{aligned} \tag{11}$$

where $x_0 = r_0\cos(\phi_0)$ and $y_0 = r_0\sin(\phi_0)$ are the Cartesian coordinates of the beam axis in the $x-y$ plane, w_1 the beam's spread in the $x-y$, w_2 the width of the dominant pulse along the z axis, A_2 the amplitude of the subdominant wave modes, P_0 the peak pressure. This model approximates the far-field plane wave produced by a circular transducer with Gaussian apodization.

The EIT forward problem given in (2) is simple to solve numerically via simulations utilizing a Finite Element Method (FEM). To optimize the electrode position, it will be convenient to consider a simplified problem with regular geometry and BCs to allow for an analytical solution that can be quickly and easily evaluated without recourse to simulations. This provides physical intuition into the forward problems' dependence on the local conductivity and the effect of geometry and electrode placement. The model should approach the CEM solution in the appropriate limit and can be easily combined with the US model given above to define a simplified AET forward problem.

Consider a cylinder of radius b, and height h (dimensions (b, h)) with constant conductivity σ_0 and a single pair of rectangular injection electrodes located along the body of the cylinder. The potential, Φ satisfies the generalized Laplace equation with the homogeneous Neumann boundary conditions in z $j = -\vec{J} \cdot \hat{n} = 0$ at $z = 0, h$ in z and the simplified Neumann BCs of constant current density $j = \frac{I_{inj}}{l_z l_\phi}$ along each electrode and zero elsewhere. Working in cylindrical coordinates, (ρ, ϕ, z) (where ρ is the usual polar radius in the x-y plane, ϕ is the corresponding polar angle, and z is the Cartesian z coordinate) the BCs are:

$$\begin{aligned} j_\rho &= \sigma_0 \vec{\nabla}\Phi \cdot \hat{\rho} = f(\phi, z) \\ &= \frac{I_{inj}}{2 z_e b \phi_e} \begin{cases} 1 & \text{if } z_e \le z - z_0 \le z_e, \phi_e \le \phi - \phi_0 \le \phi_e \\ -1 & \text{if } z_e \le z - z_1 \le z_e, \phi_e \le \phi - \phi_1 \le \phi_e \\ 0 & \text{otherwise.} \end{cases} \\ j_z &= \sigma_0 \vec{\nabla}\Phi \cdot \hat{z} = 0; \end{aligned} \tag{12}$$

The potential inside the cylinder can be expressed in terms of modified Bessel functions (I_m and K_m):

$$\begin{aligned} \Phi(\rho, \phi, z) &= V_{00} + \sum_{m=-\infty}^{\infty} \sum_{n=0}^{\infty} A_{mn} R_n(\rho; m) C_m(\phi, z; n) \\ &= V_{00} + \sum_{m=0}^{\infty} \sum_{n=0}^{\infty} R_n(\rho; m) \left(a_{mn} \cos(m\phi) + b_{mn} \sin(m\phi) \right), \end{aligned} \tag{13}$$

where

$$\begin{aligned} C_m(\phi, z; n) &= e^{im\phi} \cos(k_n z) & R_{0m}(\rho) &= \rho^m \\ R_{n>0m}(\rho) &= I_m(k_n \rho) & k_n &= \frac{n\pi}{h} \end{aligned}$$

and the A_{mn} are given in Appendix I. V_{00} is an arbitrary parameter that corresponds to the potential's ground.

Introducing a cylindrical inclusion of dimensions (a, h) with conductivity σ_1, the general solution becomes:

$$\begin{aligned} \Phi_I(\rho, \phi, z) =& A_{0,0} + V_{00} + \\ & \sum_{m=-\infty}^{\infty} \sum_{n=1}^{\infty} A_{mn} R_n(\rho) C_m(\phi, z; n) \ \ \rho < a \\ \Phi_{II}(\rho, \phi, z) =& \tilde{A}_{0,0} + \\ & \sum_{m=-\infty}^{\infty} \sum_{n=0}^{\infty} \tilde{A^i}^c_{m,n} R^i_n C_m(\phi, z; n) \ \ \rho > a, \end{aligned} \tag{14}$$

where $R^1_0 = \rho^m$, $R^2_0 = \rho^{-m}$, $R^1_{n>0} = I_m$, $R^2_{n>0} = K_m$, and the constants are given in Appendix I. The coordinate system and setup are shown in Fig. 2. As the normalization of the coefficients includes the derivative of a modified Bessel function evaluated at the boundary, the convergence of the series has a strong dependence on ρ. For $\rho < b$, the series converges quickly, its convergence being dominated by the factor of $\frac{I_m(k_n \rho)}{I'_m(k_n b)}$ in the A_{mn}. For e.g. it reaches a relative error of $\mathcal{O}(0.1\%)$ after only 10 terms in both n and m for $\rho = 0.9b$. As $\rho \to b$, the convergence slows, and the A_{mn} goes to zero as $\frac{1}{n^2 m}$.

IV. Model Validation

A. Simulation Scenarios

To validate and compare the ability of the analytical model to approximate the CEM, the results of the model are compared to a FEM simulation. The phantom used to calculate the error in the potential is a cylinder with dimensions $(1.5, 1.2)$ m with either 2 attached electrodes (when comparing the calculated EIT potential) or 4 (two injections and two measurements when comparing the AET signal). An example of this simulated experimental setup is shown in Figure 2. For simplicity, the electrode positions are fixed for each comparison, with the injection electrodes arbitrarily placed 180 degrees apart in the $z = 0.5$ and $z = 0.7$ planes for the EIT validation. The CEM is calculated using the EIDORS Matlab software package [27], [28] with a minimum element size of 0.08. The electrode impedance is taken to be 1 $\frac{S}{m}$ with an injection current of 1 Amp. Using 4 attached electrodes, electrodes 1 and 2 are driven with a 1 Amp current while the resultant voltage is measured between 3 and 4.

For the AET signal, a simplified model of the US wave is used. This US wave model is compared to a propagating far-field pulse from an idealized flat transducer simulated using Field-II [29], [30]. Field II is a C-program with a Matlab interface that can easily be interfaced with EIDORS. It does not require an internal spatial mesh in its simulation (instead relying on linear spatial impulse responses). A single-element concave transducer is simulated with a diameter of 19 mm, and a focal length of 300 m (i.e. infinity to simulate the unfocused plane wave case) with an element size of 1 mm. The excitation consisted of a single period of a 1.6 MHz sinusoid with a Gaussian weighting, scaled to produce a peak pressure of 2.6 MHz. As EIDORS calculates the EIT Jacobian for a given conductivity mesh, given the assumption of constant pressure along each mesh element, the simulated AET signal can be calculated directly from (8) while the analytical AET signal can be found by integrating (6). The integrand can be integrated analytically term by term, utilizing the fact that all functions have well-defined power series over the ranges. This allows for a code that runs extremely fast.

B. Numerical validation of the potential

The most comprehensive comparison between the calculated and simulated EIT forward problems is to compare the simulation and model at each FEM node. The relative error between the model and the FEM simulation is shown in Figure 3 for the homogeneous case. As expected, the models agree to relatively high precision for smaller radii. The model begins to diverge at

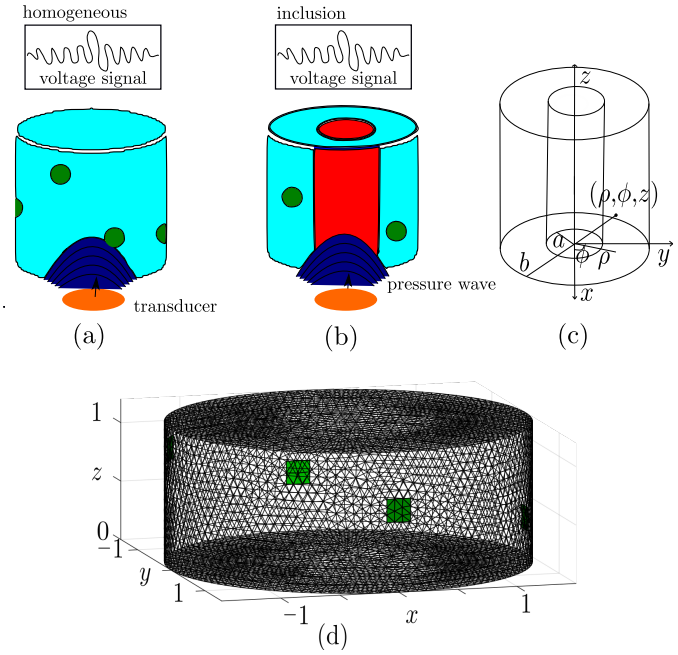

Fig. 2. Pictorial representation of the numerical experiments. Two setups are considered: In (a), a phantom with uniform conductivity where the homogeneous AEE voltage signal is measured, and in (b), a phantom with constant background conductivity with a cylindrical inclusion where the heterogeneous AEE voltage signal is measured. The cylindrical coordinates considered in this paper are defined in (c). In each setup an US pressure wave travels through the phantom generating AEE signal, the strength of which depends on the electrode placement. An example of a FEM simulation of the homogeneous cylindrical phantom is shown in (d).

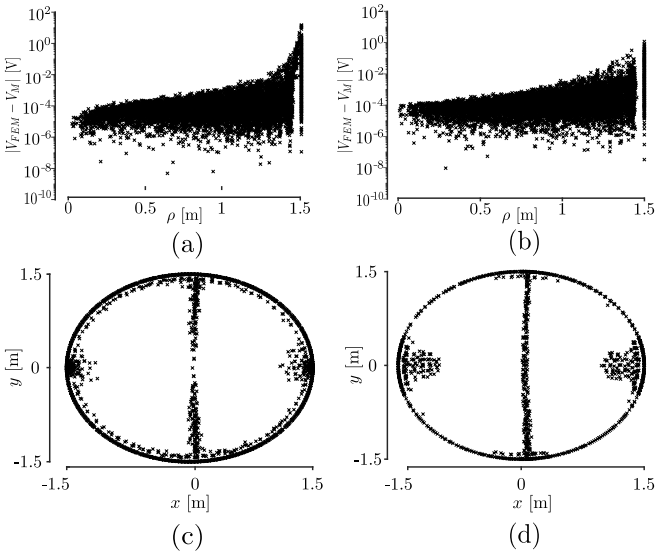

Fig. 3. Comparison between the analytical model and FEM CEM. The sum in (13) was truncated after 40 terms in both $\boldsymbol{m}$ and $\boldsymbol{n}$. In addition, the $\boldsymbol{V_{00}}$ term is not fixed using Neumann BCs and was set to be equal to the FEM node at the smallest radius. The disagreement between FEM and the model at each node of the FEM is shown. (a) Absolute value of the error (1 cm by 1 cm electrodes). (b) Absolute value of the error (10 cm by 10 cm electrodes). (c) Distribution of large relative errors ($> \mathbf{0.5\%}$ in the xy-plane for 1mm by 1mm electrodes. (d) Distribution of large relative errors ($> \mathbf{0.5\%}$ in the xy-plane for 5mm by 5mm electrodes.

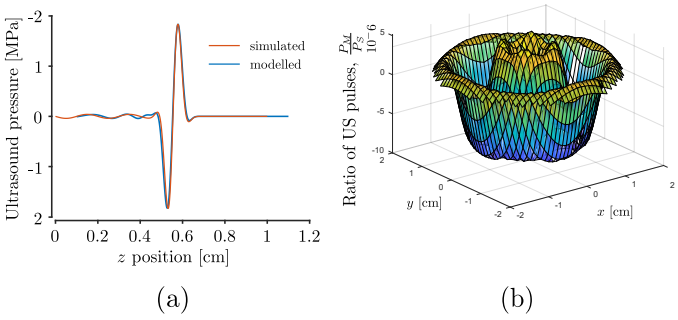

Fig. 4. Comparison between the simplified US model and a simulation of a single-element concave transducer, with a diameter of 19 mm, a focal length of 300 m with an element size of 1 mm. The excitation consisted of a single period of a 1.6 MHz sinusoid with a Gaussian weighting, scaled to produce a peak pressure of 2.6 MPa. (a) The difference between the simulated and modelled pressure waves in the $\boldsymbol{x-y}$ plane. (b) The pressure wave along $\boldsymbol{z}$ on the beam axis in the model and the simulation.

the boundary where the difference in BCs becomes significant, and where one would expect to see FEM errors. Fig. 3 also shows the distribution of nodes with large relative errors in the x-y plane. The error increases by about an order of magnitude between the small 1 cm $\times$ 1 cm electrodes and the larger 50 cm $\times$ 50 cm electrodes. As can be seen, the analytical model is quite accurate for $\rho << \mathrm{b}$ and begins to diverge at the boundary. As expected, the disagreement increases as the electrode size increases but it is still fairly accurate for small radii. The only exception to this is the zero-line of the potential (in this case along $x = 0$). This is a result of irreducible errors in the FEM which prevent it from becoming arbitrarily small. As, this is not the case in the model the disagreement along this line is expected and can be ignored.

C. Validation of US model

In Fig. 4, the model of the US pulse is compared to a pulse from a simulated transducer. It compares the x-y spread of the pressure wave in the far field ($z = 8$ cm) and the pressure along $x = y = 0$ as a function of z for two different time points. The $x - y$ spread of the model lacks the periodicity and slight non-symmetry of the simulated pulse but as these a extremely subleading effects (0.0001% of the peak) they can be safely ignored. The parameters are chosen to be: $f = 8$ MHz/mm, $w_2 = 0.46$ mm, $x_0 = 0$, y_0=0, $w_1 = 9$ mm, and P_0 was chosen to correspond to the peak pressure of the simulated wave at a particular time point. The sinusoidal tail of the US wave is modelled by a low-frequency sine wave multiplying a Heaviside step function. As its effect on the AEE signal is quite small, the coefficient of this term is set to zero for computational efficiency. The AET signal can be calculated from (8) and (6) for the FEM and the model respectively. An example calculated waveform is shown in Figure 5. In both cases shown, the injection and measurement electrodes are placed at different z-planes. For the larger cylinder, the (pointlike) injection electrodes at $z = 1$ mm and the (pointlike) measurement electrodes at $z = 99$ mm while there are placed at $z = 3$ mm and $z = 5$ mm for the small cylinder. The electrode pairs are positioned at 0 and 180 degrees respectively. In order to maximize the

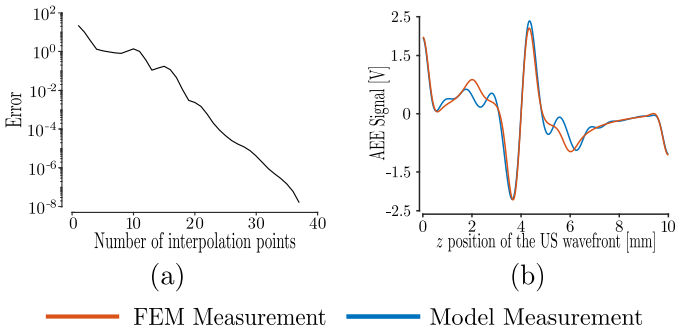

Fig. 5. Comparison of the AET waveform in the model for two different geometries. (a) The rate of convergence of the FEM AET waveform in a (10 cm,10 cm) cylinder. The error is defined as: $\boldsymbol{E} = \sum_{\boldsymbol{t}} \left(\boldsymbol{V_t^{FEM_p}} - \boldsymbol{V_t^{FEM_{38}}}\right)^2 / \left|\boldsymbol{V_t^{FEM_{38}}}\right|$ where the sum is over all time points. Though it is not shown, it approaches the analytical model. (b) The AET waveform in a (1 cm,1 cm) cylinder (plane wave case) was calculated using the FEM and the analytical model truncating the sums at 110 terms.

agreement, the FEM electrode size was chosen to be a 2 mm $\times$ 2 mm rectangle with the impedance set to 1 Ω. Electrode size effects introduce significant deviations between the models. To minimize these effects, the optimal electrode size for the analytical model electrode size determined by the least squares fit to be a 1.59 mm $\times$ 2.1 mm. These optimized electrode sizes can also absorb some disagreement due to FEM mesh size effects. While there is some disagreement between the models, the major features of the signals are the same.

V. Properties of the AEE Signal and Dependence on Electrode Position

The model, presented and validated above, gives a significant amount of insight into the AET forward problem as it allows for analytical analysis of the homogeneous AEE signal's dependence on electrode position, the US properties, and the medium's conductivity. The nature of the eigenexpansion somewhat obscures the signal's dependence on electrode position but still allows one to determine the symmetries that will maximize or minimize the signal strength. For the heterogeneous case, a term-by-term comparison with the homogeneous case allows one to determine the result of the competition between the EIT sensitivity and the AEE coupling.

A. Homogeneous Case

From (6) and (2), the AEE signal is given by:

$$\begin{aligned}\delta V_{AEE} = k\sigma_0 \int_0^b \int_0^{2\pi} \int_0^h P(\rho,\phi,z,t)\rho d\rho d\phi dz \\ \sum \nabla\left[A_{m_{In}n_{In}} R_{n_{In}}(\rho) C_{m_In}(\phi,z;n_{In})\right] \\ \cdot \nabla\left[A_{m_Mn_M} R_{n_M}(\rho) C_{m_M}(\phi,z;n_M)\right].\end{aligned} \tag{15}$$

To describe the scaling of the signal and its temporal waveform as a function of electrode position and the US beam axis and beam spread, it is necessary to expand out the dot product in (15) and describe the various terms at each order in the eigen-expansion. This expansion can be parameterized as:

$$\begin{aligned}\delta V_{AEE} = \int P(\rho,\phi,z,t)\rho d\rho d\phi dz \\ \left[R_p(m,n)^2 A(m,n)^2 Z(n)^2\right. \\ + R(m,n)^2 A_p(m,n)^2 Z(n)^2 \\ \left.+ R(m,n)^2 A(m,n)^2 Z_p(n)^2\right]\end{aligned} \tag{16}$$

where e.g. $A(m,n)^2 = A(m_{In},n_{In})A(m_M,n_M)$, the subscript p represents the derivative coming from the gradient, and there is an implicit sum over the $m = m_M, m_{In}$, and $n = n_M, n_{In}$. The naive expectation is that the higher order terms in this sum will be suppressed by the coefficients, $A_{m_Mn_M}$. However, $A_{m_Mn_M}$ is gives an

$$A_{m_Mn_M} \sim \frac{\sin(k_n z_e)}{k_n^2}\frac{\sin(m\phi_e)}{m},$$

is partially cancelled by factors of k_n and m introduced by the differentiation. In any case, the dominant source of suppression of higher modes comes from the $\rho\phi$ integration, represented above by the RA functions. This is especially relevant for small electrodes, as the factor of e.g. $\sin(k_n z_e)$ will cancel out another factor of n^{-1} suppression while $\phi_e << n\pi/h$. In this case, the higher n (and m) modes are not suppressed via the coefficients in the eigen-expansion, but by the $\rho\phi$ integration. Since the waveform is determined by the relative suppression between z-modes (resulting from the z integration, in this case the shape of the AEE signal is dominated by the geometry of the cylinder, not the electrode placement. An advantage of this analytical approach is that these integrals can be formally calculated within the model giving additional insight into the AEE signal's dependence on the cylinder's dimensions. For the details, see the supplemental Appendix. Both the z and the angular integration can be done analytically. This integration distinguishes two cases; the simple case with angular symmetry with only involves the same m-modes (i.e. all terms vanish except when $m_{In} = m_M$) and the case where the beam axis is off-center which mixes the different m-modes together and opens up additional cross-terms between the $n = 0$ and $n > 0$ modes. In general, the off-center integration results in an enhancement of modes $m = m_1 + m_2$ where m_1 and m_2 are close together and suppression of the modes where they are far apart.

While the final ρ integration lacks a closed form solution, the form of its power series, ensures that the higher order modes are suppressed, though the speed of this suppression is strongly dependent on the relative values of w_1 and b as well as the radial function. For the $n = 0$, $m > 1$ modes, the radial function is simply

$$R(m,0) = \rho^{m_{In}+m_M-1}$$

and the higher m modes are suppressed by factors of

$$m_{In}m_M\left(\frac{w_1}{b}\right)^{m_{In}+m_M}$$

For $n > 0$ modes, the $A_{mn} \sim \frac{1}{I'_m(kn\rho)}$ and the effect of ρ integration is to truncate the power series of the numerator

$$\frac{I_{m_{In}}(kn_{In}w_1)I_{m_M}(kn_Mw_1)}{I'_{m_{In}}(kn_{In}b)I'_{m_M}(kn_Mb)}.$$

If $b >> w_1$, this truncation occurs rapidly and combined with each term in the sum of the numerator is already suppressed by $\left(\frac{w_1}{b}\right)^n$ relative to the corresponding term of the sum in the denominator only a few n modes contribute to the AEE signal. If $w_1 \sim b$, the truncation occurs very slowly and therefore more modes need to be included.

For the higher m modes, in addition to the above effect suppression, there is also a suppression of $\mathcal{O}(w_1^{mIn+mM})$, which is similar to the suppression in the $n = 0$ modes. This implies that the naive expectation is that for a sufficiently large radius, the $n = 0$ modes will dominate the waveform unless they are suppressed by the placement of the electrodes, which determines the numerator of the A_{mn}.

As the beam axis moves away from the origin, the angular integration introduces a Gaussian suppression of the form $\exp\left(r_0^2/w_1^2\right)$, which makes this approach an impractical way to perform the integration. It does however clearly demonstrates that moving the beam axis away from the origin will not drastically change the order by order suppression though it does allow for additional combinations of A_{mn} in the numerator, which will change how the electrode placement affects the signal strength and the selection of the dominate z modes. This Gaussian suppression also implies that the sensitivity to tightly focused beams will be suppressed as the beam approaches the boundaries.

B. Heterogeneous Case

The behaviour of the heterogeneous AEE signal relative to the homogeneous case can be understood by rearranging (24)-(26). The behaviour in the case where the US probe is focused within the inclusion is quite similar to the homogeneous case as the potential has the same functional dependence on ρ. Using the constants given in Appendix I, the $n = 0$ modes of the potential (which describe the ρ^m terms) can be written:

$$\Phi_{m0}^{\text{inc}} = \Phi^{\text{homo}} \frac{1}{\Delta}\left(1 + \left(\frac{a}{b}\right)^{2m} \frac{1}{\Delta'}\right)^{-1}, \tag{17}$$

where

$$\Delta = 1 + \frac{\sigma_1 - \sigma_0}{2\sigma_0}, \qquad \text{and} \qquad \Delta' = 1 + \frac{2\sigma_0}{\sigma_1 - \sigma_0}.$$

As m increases, the conductivity dependence approaches $\frac{1}{\Delta}$. Similarly, the $n > 0$ modes can be written:

$$\Phi_{mn}^{\text{inc}} = \Phi^{\text{homo}}\left(1 + \frac{(1 - R'_m(\sigma_1 - \sigma_0)}{(1 - R)\sigma_0}\right)^{-1}, \tag{18}$$

where

$$R_m = \frac{K'_m(k_n a)}{K_m(k_n a)} \frac{I_m(k_n a)}{I'_m(k_n a)}$$

which is $R_m \approx -1.4$ for $m = 0$, goes to -1 as m and n increase, while

$$R'_m = \frac{K'_m(k_n b)}{K_m(k_n a)} \frac{I_m(k_n a)}{I'_m(k_n b)} \tag{19}$$

goes to zero in the same limit. As m and n increase, this approaches the same limit as the ρ^m terms. As the sensitivity is given by $\sigma E \cdot E$, the sensitivity approaches

$$S = \frac{4\sigma_1}{(\sigma_0 + \sigma_1)^2} \tag{20}$$

taking into account the $\frac{1}{\sigma_0}$ dependence of Φ^{homo}. When $\rho > a$, the radial modes that diverge at the origin must be included, which opens up additional radial dependencies. For the $n = 0$ modes $\rho^m + \rho^{-m}$, the potential is:

$$\begin{aligned}\Phi_{m0}^{\text{inc}} &= \Phi^{\text{homo}}\left(1 - \frac{a^{2m}}{\rho^{2m}\Delta'}\right)\left(1 + \frac{a^{2m}}{b^{2m}\Delta'}\right)^{-1} \\ E_{\rho m0}^{\text{inc}} &= E_\rho^{\text{homo}}\left(1 + \frac{a^{2m}}{\rho^{2m+1}\Delta'}\right)\left(1 + \frac{a^{2m}}{b^{2m}\Delta'}\right)^{-1}.\end{aligned} \tag{21}$$

Similarly for the $n > 0$ modes, the potential goes as:

$$\begin{aligned}\Phi_{m0}^{\text{inc}} &= \Phi^{\text{homo}}\left(\left[1 - \frac{R_{\rho m}}{1 + \frac{F\sigma_0}{\Delta\sigma}}\right]\left[1 - \frac{R'_m}{1 + \frac{F\sigma_0}{\Delta\sigma}}\right]\right)^{-1} \\ E_\rho^{\text{inc}} &= E^{\text{homo}}\left(\left[1 - \frac{R'_{\rho m}}{1 + \frac{F\sigma_0}{\Delta\sigma}}\right]\left[1 - \frac{R'_m}{1 + \frac{F\sigma_0}{\Delta\sigma}}\right]\right)^{-1}.\end{aligned} \tag{22}$$

where

$$\begin{aligned}R_{\rho m} &= \frac{K_m(k_n\rho)}{K_m(k_n a)} \frac{I_m(k_n a)}{I_m(k_n\rho)} \qquad \Delta\sigma = \sigma_1 - \sigma_0 \\ R'_{\rho m} &= \frac{K'_m(k_n\rho)}{K_m(k_n a)} \frac{I_m(k_n a)}{I'_m(k_n\rho)} \qquad F = (1 - R_m).\end{aligned}$$

The behaviour of the signal as a function of conductivity is much more complicated than the $\rho < a$ case. As the radius increases, the conductivity dependence cancels, and the enhancement or suppression for higher-order terms approaches zero. As σ_1 increases, there is always an enhancement of the ρ; $n > 0$ modes since

$$\begin{aligned}R'_m &\leq R'_{\rho m} \\ K'_m(x) &< 0.\end{aligned}$$

Conversely, the ϕ and z $n > 0$ modes are always suppressed, as $0 < R_{\rho m} \leq 1$ and $R_m < 0$. For the $n = 0$ modes, there is radial enhancement if $\rho > b^{\frac{2m}{2m+1}}$ and a suppression otherwise. If $\sigma_1 < \sigma_0$ this pattern is reversed. In general, this implies suppression as σ_1 increases and enhancement as it goes to zero.

In summary, as the US pulse passes through an inclusion, there will always be an approximately global suppression (enhancement) of the signal relative to the homogeneous case as the inclusion conductivity increases (decreases). There is a mode-by-mode dependence, which washes out for the higher modes. This will slightly alter the waveform as the lower modes are somewhat suppressed relative to the higher modes. The effect will thus be most significant for signals which are dominated by the lower modes. As the US wave pulse reaches the boundary of the inclusion, there can be an enhancement to the signal, depending on the relative importance of the radial modes of the electric field. Away from the inclusion, the signal approaches the homogeneous limit.

The observed behaviour always applies to a setup with cylindrical symmetry. While this setup represents the minimal implementation of AET, any practical application will certainly involve more complex geometries. It is important to therefore understand how the above conclusions generalize to other geometries. As summarized in Section V-C,

Fig. 6 and 7, the observed signal depends drastically on the eigenfunction expansion, i.e., if the dominant mode is maximized or suppressed. On the other hand, the behaviour of the signal discussed in this section depends primarily on the patterns between the modes of the eigen-expansion and are applicable to more general situations. Since in this case the eigen-expansion must be calculated numerically, the physical intuition derived from the simplified model should be particularly useful in these cases.

C. Results

The AEE signal strength is a function of the cylinder's dimensions, the electrode placement, and the US beam axis. The cylinder's geometry determines the relative suppression of the different z-modes of the AEE signal, which is constant for every combination of electrode and US beam placement. The electrode placement scales the relative contributions of the $\cos$ and $\sin$ z modes. In principle, there is a functional dependence, determined by the geometric suppression. If the cylinder radius is sufficiently large, on the order of a couple of cms, the leading terms will dominate and the functional dependence reduces to a more simplified dependence. Regardless, certain choices of angular or z symmetry can force the contributions of different modes to zero. For example, placing the measurement or injection electrodes at the same angular position will remove the $n = 0$ modes. Similarly placing the electrodes along the same z-plane removes the $m = 0$ modes. The effect on the AEE signal is shown in Fig. 7.

The effect of the AEE signal of changing the conductivity for the case with inclusion is shown in Fig. 6. Two different behaviours are investigated. The behaviour of the signal of a central US pulse as a function of conductivity and radius of the inclusion. The functional dependence on the conductivity generally follows the naive expectation derived above. To show this, Fig. 6 gives an example case, where the electrode pairs are placed at 0 and 180 degrees with the injection (measurement) at $z = 0.2h$ mm ($z = 0.8h$ mm). Since the signals are dominated by the lower modes which for the US pulse considered produce sharp peaks as the pulse enters and exits the cylinder, the peak signal including and excluding these peaks are included. The peak signal, dominated by the lower modes, goes to zero as $\sigma_1 \to 0$ as expected by the approximate $\frac{\sigma_1}{(\sigma_0+\sigma_1)^2}$ while the peak signal near the electrodes increases as it is more sensitive to changes in the relative contribution these modes and the enhancements caused by the $\rho > a$ integration. Since the higher modes are less suppressed for the thinner cylinder, these effects are much stronger and the signal strength is enhanced for almost all conductivities. The dependence of the peak signal on the radius of the inclusion follows a similar pattern. The effect on the peak signal is muted but there are significant enhancements to the signal away from the edges where the $\rho > a$ enhancements dominate. Fig. 6 also includes the results of a scan over 1500 random electrode positions. The only requirement on the electrode positions where that they was a minimum distance $0.05b$ separating each electrode. The 3rd and 4th panels of Fig. 6 give the results of this scans, showing the maximum, minimum, and mean ratio of the peak inclusion signal to the peak homogeneous signal for the same electrode placement. They show that while enhancements are possible, especially for the thinner cylinder, the competition between the AEE and EIT tends to result in mean suppression of the signal, which approaches 60% as conductivity of the inclusion reaches 8 S/m and as the radius of the inclusion increases. The results shows that the schematic relationship between AET sensitivity and anomaly conductivity sketched out in Fig. 1 generally holds but in rare cases the suppression of the sensitivity of the anomaly is out competed by the effect of current flow in the homogeneous background. The 5th and 6th panels of Fig. 6 show the ratio maximum and mean suppression (or enhancement) of the inclusion voltage signal excluding the edges to the peak of the largest homogeneous signal of all scan points, not the corresponding point in the scan as in Figs. (5c) and (5d). Though it is not shown, when the homogeneous signal is small and dominated by the edges, the introduction of a inclusion can lead to large enhancements to the signal away from the edges (as large as an order of magnitude) by introducing larger wavelength oscillations into the signal. Figs. (5e) and (5f) show that while significant enhancements (i.e. up to 200%) are possible on average there is a significant suppression of the peak signal. The inclusion conductivity is chosen to cover the range of typical contrasts typically seen in biological tissue [31], [32], [33]. In particular, the choice of a contrast of 5 times the background as the reference point when showing the radial dependence is arbitrary. Figure 7 compares the peak AET waveform for two different geometries and electrode placements. The different placement is chosen to either maximize or minimize different modes to demonstrate the effect of electrode placement on the AEE signal. The electrodes configurations are: Configuration 1) Electrodes are placed along 2 z-planes (a injection plane and a measurement plane) a distance d apart at 0 and 180 degrees respectively (where $d = 0$ corresponds both the injection and measurements lying along the $z = 0.5h$ mm plane. Configuration 2) Electrodes are placed along the $z = 0.5h$ mm plane, each measurement and injection pair 180 degrees apart with an angular offset ϕ between the first measurement electrode and the first injection electrode. Configuration 3) The injection electrodes are placed along the $\phi = 0$-plane and the measurement electrodes along $\phi = 180$ plane; the 1st injection and measurement electrodes are placed on the $z = 0.5h$ mm plane while the second injection and measurement electrodes are placed along a variable z-plane. The two cylinder's are a (100 mm,100 mm) cylinder and a (200 mm,40 mm) cylinder respectively. The differences between the results for each cylinder highlights the importance of higher higher order modes for cylinders where the radius is small compared to the height. The first configuration shows how the signal scales as a function of distance between injection and electrodes. The second configuration highlights the strong dependence of the signal sensitivity to angular symmetries while the third minimizes the normal leading order dominant modes, demonstrating the importance in electrode placement on the signal strength.

Finally, Fig. 8 shows the dependence of the radius on the

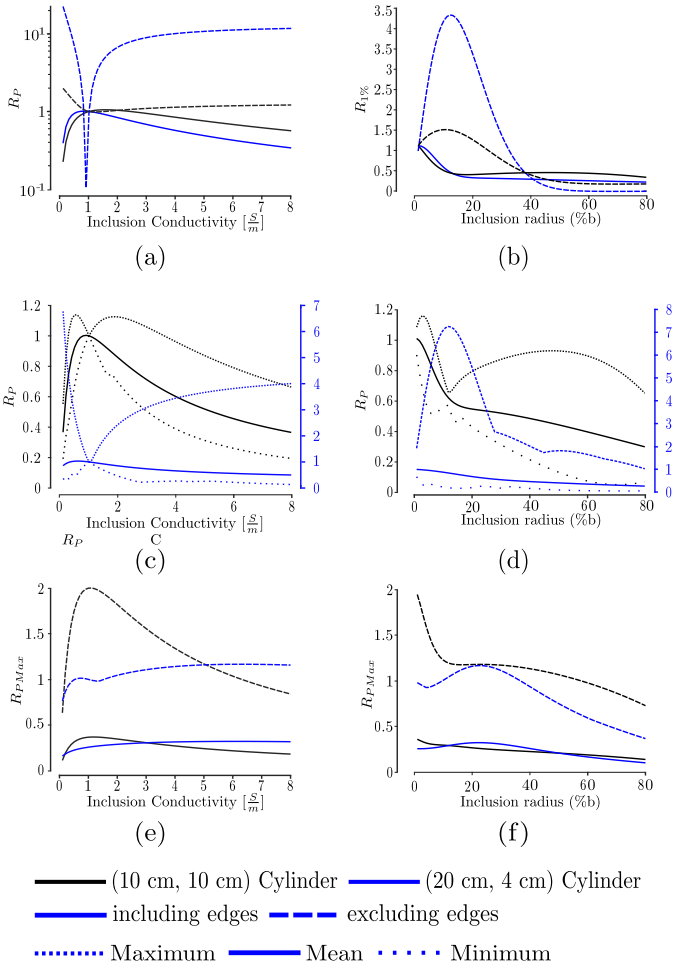

Fig. 6. The dependence of ratios of the peak AEE signal as a function of the inclusion for electrodes for a (100 mm,100 mm) and (200 mm,20 mm) cylinder. $\boldsymbol{R_P}$ is the ratio of the peak inclusion signal to the peak homogeneous signal for a given electrode configuration. $\boldsymbol{R_{1\%}}$ is the peak inclusion signal normalized to $\boldsymbol{a = 1\%b}$. $\boldsymbol{R_{PMax}}$ is the ratio of the peak inclusion signal to the maximum peak homogeneous signal of all scan points. (a) Variable conductivity and a fixed inclusion radius of $\boldsymbol{\rho_i = 0.3b}$ mm for a single electrode configuration. (b) Variable inclusion radius and a fixed conductivity of 5 S/m for a single electrode configuration. (c) Variable conductivity and a fixed inclusion radius of $\boldsymbol{\rho_i = 0.3b}$ mm over a scan of random electrode configurations. (d) Variable radius and a fixed conductivity of $\boldsymbol{5}$ S/m over a scan of random electrode configurations excluding the signal's edges. (e) Variable conductivity and a fixed inclusion radius of $\boldsymbol{\rho_i = 0.3b}$ mm over a scan of random electrode configurations. (f) Variable radius and a fixed conductivity of $\boldsymbol{5}$ S/m over a scan of random electrode configurations excluding the signal's edges.

xy-integration. As the xy-integration generally determines the order at which higher z modes are cut-off, the relative size of these terms, which captures the effect of the cylinder geometry on the signal, can have a large impact on the AEE signal. Two cases are shown. One where the cylinder radius equals the height and another where the radius is half the height. In summary, this analysis reveals three important observations:

- Electrode placement is essential to maximizing the AEE signal's amplitude and the signal acquisition in a realistic minimal AET setup.
- For a cylindrical model, the ratio of the radius to the height is the main driver of both the maximum signal

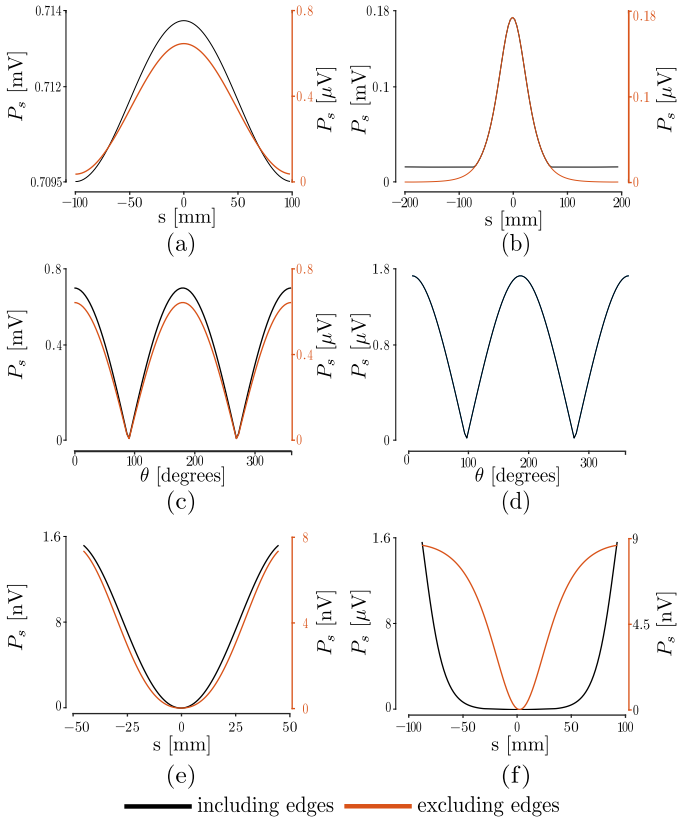

Fig. 7. Comparison of the peak homogeneous AET waveform in the model for two different geometries and three choices of symmetric electrode placements. (a) A (100 mm,100 mm) cylinder with placement 1). (b) A (200 mm,40 mm) cylinder with placement 1). (c) A (100 mm,100 mm) cylinder with placement 2). (d) A (200 mm,40 mm) cylinder with placement 2).(c) A (100 mm,100 mm) cylinder with placement 3). (d) A (200 mm,40 mm) cylinder with placement 3).

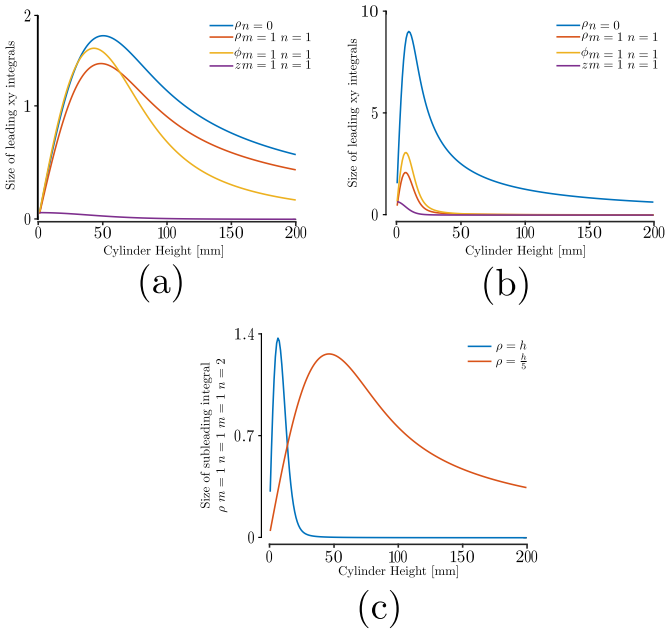

Fig. 8. Size of the leading $\boldsymbol{xy}$ integration as a function of cylinder radius for a cylinder of dimensions $(\boldsymbol{h},\boldsymbol{h})$ and $(\boldsymbol{h},\frac{\boldsymbol{h}}{\boldsymbol{5}})$. (a) The leading terms for a $(\boldsymbol{h},\boldsymbol{h})$ cylinder. (b) The leading terms for a $(\boldsymbol{h},\frac{\boldsymbol{h}}{\boldsymbol{5}})$ cylinder. (c) The subleading n=2 term for integration of the $\boldsymbol{m = 1; n = 1; m = 1; n = 2}$ of the $\boldsymbol{E_\rho \cdot E_\rho}$ term for a $(\boldsymbol{h},\boldsymbol{h})$ and a $(\boldsymbol{h},\frac{\boldsymbol{h}}{\boldsymbol{5}})$ cylinder.

amplitude and the relative size of the waveform's peaks.
- Despite the potential for a strong cancellation between the conductivity dependence of the linear AEE coupling and the EIT sensitivity, the AEE signal retains a strong dependence on the conductivity.

VI. Discussion

The model of the AET forward problem given by (8) has the potential to be a useful parameterization for solving the AET inverse problem. The form of (8) has two main implications for the AET problem. Firstly, since the signal is proportional to the EIT Jacobian, areas of a body with zero sensitivity for EIT should still have zero sensitivity in AET. Secondly, and more importantly, the effect of the EIT Jacobian seemingly competes with the AEE effect, washing out the naively expected linear dependence on σ. The approximate form of the Jacobian,

$$J^{EIT} = \sigma|E|^2 \approx \frac{|j|^2}{\sigma}$$

combined with a first-order approximation of local current flow results in an exact element-by-element cancellation between the conductivity dependence of the AEE and the EIT sensitivity. If this held to higher orders, the signal would be determined by the geometry of the target and the form of the pressure wave. If the AEE signal is dominated by the geometry of the body, it would make it quite difficult to solve the inverse problem with a small number of EIT measurements (as opposed to using a larger number of measurements to reconstruct the boundary potential as in [19]).

Furthermore, the main advantage of this approach to the AEE problem is that the mesh used to discretize the conductivity can be used to simulate the pressure wave. This mesh is large compared to the scale of a focused US pulse, so it is important to determine the FEM mesh size required to accurately model the AET forward problem. Fig. 5 shows the comparison between the FEM simulation and the simplified analytical model. While the strong agreement between the FEM and model potential within the area probed by the US pulse suggests that the model and simulation of the AEE signal could agree to similar precision, the different BCs prevent this as electrode effects play an important role in the calculation of the Jacobian. Despite this, the comparison shows that the analytical model is a reasonable proxy for the FEM simulation, validating both the FEM simulation and the model. Also shown in Fig. 5 is the additional mesh interpolation of the US pulse needed before the FEM converges to a stable result. The maximum mesh size in the FEM simulation is 1 mm, suggesting the US pulse needs to be calculated to a fitness of approximately 0.05 mm. The computational power required to make a full simulation of the AET forward problem should therefore be well within the reach of a decent personal computer.

The agreement between the FEM simulation and the model also suggests that the physical intuition gleaned from the model as well as the results given in Fig. 7 related to signal strength will apply equally well to the more realistic FEM. While the signal is generally quite small, choices in the geometry of the body and the placement of the electrodes can greatly help or hinder an experimental attempt to reliably observe the AEE, an essential step for any practical minimal AET system.

This work suggests that for a cylindrical object, the signal should be strongest for objects whose height is large relative to their radius. Without recourse to symmetry to suppress particular modes, the signal was generally dominated by the time points corresponding to the US pulse entering and leaving the body. This feature can largely be attributed to the use of a perfectly symmetric US pulse. While assymmetries in the pulse will most likely result in a washing out of this effect, it provides an additional mechanism to enhance the AEE signal as the US pulse enters an inclusion. Ignoring this boundary effect, the model implies that the optimal electrode placement for the injection or measurement electrodes should be along the same z-plane, 180 degrees apart (i.e. maximally spaced) with the two z-planes close together. The ideal separation is most likely half the US pulse wavelength so that as the pressure wave passes through the electrode planes, the positive peak is aligned with one plane and the negative peak with the other. This does not seem to be a particularly practical setup for most applications of AET, but is definitely feasible in an application involving e.g. biopsy needles which are also instrumented as EIT electrodes.

The model shows that the local conductivity dependence of the AEE signal does not cancel as a naive parameterization of (8) would imply. Though the signal maintains a strong dependence on the geometry of the cylinder and the US beam axis, the AEE signal when the inclusion is being probed, also has a strong order-independent conductivity dependence that tends to enhance the signal when the inclusion conductivity is smaller than the background and suppresses the signal when it is larger. When the region outside the inclusion is being probed, the conductivity dependence has roughly the same dependence as the homogeneous case but there is generally an enhancement as the US probes the boundary of the inclusion. Thus both the suppression of the signal as the US pulse enters regions of higher conductivity and the enhancement at the boundary suggest that a minimal AET setup provides sufficient information to solve the inverse problem assuming the small signal can be reliably measured in vivo.

The above argument focuses on AET using a minimal setup and considers the case of the ideal AET inverse problem, i.e., one that: (1) ignores uncertainty in the US wave speed, which makes it difficult to accurately model the forward problem, and (2) assumes a signal-to-noise (SNR) ratio small enough for the signal to be reliably detected. The key quantity to determine whether a particular AET application is feasible is the signal strength; which is primarily a function of pulse strength, conductivity distribution and electrode positions. We have modeled a geometric scenario which retains these key features and incorporates the interactions between the ultrasound conductivity in 3D. This model leads to one of the easiest experimental setups where the AEE signal can be detected and the AET conductivity distribution can be reconstructed. The model then represents a reasonable best-case scenario, and can be used to test the effectiveness of AET sensors and equipment. This makes it possible to place

an upper bound on the SNR that the system needs to achieve to detect the AEE signal and realize AET. With results presented in the previous section, the upper bound can be placed by top-normalizing the signals given in Figs 6, 7 to the corresponding EIT signal, which, for the parameters considered above, is $\mathcal{O}$(10mV). Thus, a realistic AET system would need an EIT SNR of at least 1% to detect the edges of the AEE signal and an EIT SNR of 0.0001% to achieve an AEE SNR of 10%. The required uncertainty in the US propagation is more difficult to estimate, as the model requires a constant speed as the US propagates through the medium. If the US speed is constant, any uncertainty in the speed will result in a corresponding global compression or stretching of the AEE waveform. This effect should have a limited impact on the AET reconstruction compared to the effect of variable US propagation speed.

VII. Conclusion

AET is a promising technique with the potential to combine the non-invasive imaging abilities of EIT with the high resolution of US. While most research has focused on only one part of the reconstruction process, recent research has begun to turn to more realistic and concrete scenarios. These scenarios are simple 2D geometries with setups that involve a large number of EIT boundary electrodes. More minimal AET setups, which involve single pairs of injection and/or measurement electrodes have the potential to provide useful in vivo imaging in situations that involve e.g. dual purpose electrodes/biopsy needles. Before scenarios such as these can be realized, it is important to characterize and understand the AET forward problem.

This paper introduced an analytical model of the AET forward problem given simplified BCs on the injection electrodes. The model considers the case of a simple 3D geometry, a cylinder with one pair of injected electrodes and one pair of measurement electrodes. It was compared to a more realistic CEM FEM simulation of the forward problem and shown to be a reasonable proxy for the FEM simulation. Using this model, the idealized measurement voltage induced by a simplified US pulse was calculated to first order. The AEE signal was shown to have a significant dependence on the cylinder's dimensions, and electrode placement, with the optimal electrode placement consisting of a measurement z-plane and an injection z-plane separated by a minimal distance with the two measurements and injection placed at 0 and 180 degrees. The AEE signal's dependence on the conductivity of an inclusion was also investigated and it was shown that the signal's dependence on conductivity was not washed out by the competing effect of the linear AEE coupling and the $\frac{1}{\sigma}$ of the EIT Jacobian and contained enough information to allow for a solution to the inverse problem, assuming the small size of the AEE signal allows for reliable measurement.

References

[1] D. Holder and A. Adler, Eds., *Electrical Impedance Tomography Methods, History and Applications*. CRC Press, 2022.

[2] I. Frerichs *et al.*, "Chest electrical impedance tomography examination, data analysis, terminology, clinical use and recommendations: consensus statement of the translational eit development study group," *Thorax*, vol. 72, pp. 83–93, 09 2016.

[3] F. Perier *et al.*, "Electrical impedance tomography to titrate positive end-expiratory pressure in covid-19 acute respiratory distress syndrome," *Critical care (London, England)*, vol. 24, 12 2020.

[4] S. Leonhardt *et al.*, "Electrical impedance tomography for hemodynamic monitoring," in *2012 Annual International Conference of the IEEE Engineering in Medicine and Biology Society*, 2012, pp. 122–125.

[5] D. T. Nguyen *et al.*, "A review on electrical impedance tomography for pulmonary perfusion imaging," *Physiological measurement*, vol. 33, pp. 695–706, 04 2012.

[6] E. Malone *et al.*, "Stroke type differentiation using spectrally constrained multifrequency eit: Evaluation of feasibility in a realistic head model," *Physiological Measurement*, vol. 35, p. 1051, 05 2014.

[7] L. Fabrizi *et al.*, "Factors limiting the application of electrical impedance tomography for identification of regional conductivity changes using scalp electrodes during epileptic seizures in humans," *Physiological measurement*, vol. 27, pp. S163–74, 06 2006.

[8] Y. Zou and Z. Guo, "A review of electrical impedance techniques for breast cancer detection," *Medical engineering & physics*, vol. 25, pp. 79–90, 04 2003.

[9] A. Pathiraja *et al.*, "The clinical application of electrical impedance technology in the detection of malignant neoplasms: a systematic review," *Journal of Translational Medicine*, vol. 18, 06 2020.

[10] H. Zhang and L. V. Wang, "Acousto-electric tomography," in *Photons Plus Ultrasound: Imaging and Sensing*, A. A. Oraevsky and L. V. Wang, Eds., vol. 5320, International Society for Optics and Photonics. SPIE, 2004, pp. 145 – 149. [Online]. Available: https://doi.org/10.1117/12.532610

[11] H. Ammari *et al.*, "Electrical impedance tomography by elastic deformation," *SIAM Journal on Applied Mathematics*, vol. 68, 06 2008.

[12] F. E. Fox, K. F. Herzfeld, and G. D. Rock, "The effect of ultrasonic waves on the conductivity of salt solutions," *Phys. Rev.*, vol. 70, no. 5-6, pp. 329–339, Sep 1946.

[13] B. Lavandier, J. Jossinet, and D. Cathignol, "Experimental measurement of the acousto-electric interaction signal in saline solution," *Ultrasonics*, vol. 38, no. 9, pp. 929–936, 2000.

[14] J. Jossinet, B. Lavandier, and D. Cathignol, "The phenomenology of acousto-electric interaction signals in aqueous solutions of electrolytes," *Ultrasonics*, vol. 36, no. 1, pp. 607–613, 1998, ultrasonics International 1997.

[15] P. Kuchment and L. Kunyansky, "2d and 3d reconstructions in acousto-electric tomography," *Inverse Problems*, vol. 27, no. 5, p. 055013, apr 2011.

[16] B. J. Adesokan *et al.*, "Acousto-electric tomography with total variation regularization," *Inverse Problems*, vol. 35, no. 3, p. 035008, feb 2019.

[17] G. Bal *et al.*, "Inverse diffusion from knowledge of power densities," 2011.

[18] P. Kuchment and L. Kunyansky, "Synthetic focusing in ultrasound modulated tomography," *Inverse Problems &amp: Imaging*, vol. 4, no. 4, pp. 665–673, 2010.

[19] C. Li *et al.*, "A complete framework for acousto-electric tomography with numerical examples," *IEEE Access*, vol. 8, pp. 98 508–98 517, 2020.

[20] B. Jensen, A. Kirkeby, and K. Knudsen, "Feasibility of acousto-electric tomography," 2019.

[21] B. C. S. Jensen and K. Knudsen, "Sound speed uncertainty in acousto-electric tomography," *Inverse Problems*, vol. 37, no. 12, p. 125011, nov 2021.

[22] H. Zhang *et al.*, "Biological current source imaging method based on acoustoelectric effect: A systematic review," *Frontiers in Neuroscience*, vol. 16, 2022. [Online]. Available: https://www.frontiersin.org/articles/10.3389/fnins.2022.807376

[23] E. Somersalo, D. Isaacson, and M. Cheney, "A linearized inverse boundary value problem for maxwell's equations," *Journal of Computational and Applied Mathematics*, vol. 42, no. 1, pp. 123–136, 1992.

[24] K.-S. Cheng *et al.*, "Electrode models for electric current computed tomography," *IEEE transactions on bio-medical engineering*, vol. 36, pp. 918–24, 10 1989.

[25] C. Li *et al.*, "Levenberg–marquardt algorithm for acousto-electric tomography based on the complete electrode model," *Journal of Mathematical Imaging and Vision*, vol. 63, no. 4, pp. 492–502, May 2021. [Online]. Available: https://doi.org/10.1007/s10851-020-01006-y

[26] B. Lavandier, J. Jossinet, and D. Cathignol, "Quantitative assessment of ultrasound-induced resistance change in saline solution," *Med. Biol. Eng. Comput.*, vol. 38, no. 2, pp. 150–155, 2000.

[27] N. Polydorides and W. R. B. Lionheart, "A matlab toolkit for three-dimensional electrical impedance tomography: a contribution to the electrical impedance and diffuse optical reconstruction software project,"

Measurement Science and Technology, vol. 13, no. 12, p. 1871, nov 2002.

[28] A. Adler and W. R. B. Lionheart, "Uses and abuses of eidors: an extensible software base for eit," *Physiological Measurement*, vol. 27, no. 5, p. S25, apr 2006.

[29] J. Jensen and N. Svendsen, "Calculation of pressure fields from arbitrarily shaped, apodized, and excited ultrasound transducers," *IEEE Transactions on Ultrasonics, Ferroelectrics, and Frequency Control*, vol. 39, no. 2, pp. 262–267, 1992.

[30] J. Jensen, "Field: A program for simulating ultrasound systems," *Medical and Biological Engineering and Computing*, vol. 34, pp. 351–352, 01 1996.

[31] R. J. Halter *et al.*, "Electrical impedance spectroscopy of benign and malignant prostatic tissues," *The Journal of Urology*, vol. 179, no. 4, pp. 1580–1586, 2008. [Online]. Available: https://www.sciencedirect.com/science/article/pii/S0022534707030820

[32] R. Halter *et al.*, "Electrical impedance spectroscopy of the human prostate," *Biomedical Engineering, IEEE Transactions on*, vol. 54, pp. 1321 – 1327, 08 2007.

[33] E. Johnston *et al.*, "Verdict mri for prostate cancer: Intracellular volume fraction versus apparent diffusion coefficient," *Radiology*, p. 181749, 04 2019.

Appendix I
Analytical Model

The constants in the homogeneous case are given by:

$$\begin{aligned}
A_{m,n} =& \frac{I_{inj}}{\sigma_0 z_e b \phi_e k_n^2 \pi h m I'_m\left(\frac{n\pi b}{h}\right)} \sin(k_n z_e)\sin(m\phi_e) \\
& [\cos(k_n z_0)\left(-i\sin(m\phi_0)+\cos(m\phi_0)\right) \\
& -\cos(k_n z_1)\left(-i\sin(m\phi_1)+\cos(m\phi_1)\right)] \\
A_{0,n} =& \frac{I_{inj}}{\sigma_0 z_e b k_n^2 \pi h I'_0\left(\frac{n\pi b}{h}\right)} \sin(k_n z_e) \\
& [\cos(k_n z_0)-\cos(k_n z_1)] \\
A_{m,0} =& \frac{I_{inj}}{\sigma_0 b \phi_e m^2 \pi h b^{m-1}} \sin(m\phi_e) \\
& \left[-i\left(\sin(m\phi_0)-sin(m\phi)\right)+\cos(m\phi_0)-\cos(m\phi_1)\right].
\end{aligned} \tag{23}$$

Taking z_e and ϕ_e to zero yields the point electrode case which converges very slowly as $\rho \to b$. Introducing a cylindrical artifact of dimensions (b, h) with conductivity σ_1, the constants in the two regions are related via:

$$\begin{aligned}
\tilde{A}_{mn} &= \tilde{B}_{mn}\frac{\sigma_1}{\sigma_0-\sigma_1}\left[\frac{K(k_n a)}{I(k_n a)}-\frac{\sigma_0}{\sigma_1}\frac{K'_m(k_n a)}{I'(k_n a)}\right] \\
\tilde{A}_{mn} &= \tilde{B}_{mn} \\
B\tilde{A}^c_{m0} &= \tilde{B}^c_{m0}B_0 \\
\tilde{A}^s_{m0} &= \tilde{B}^c_{m0}B_0 \\
\tilde{A}^c_{m0} &= \frac{\tilde{B}^c_{m0}}{a^{2m}}\left(\frac{\sigma_0+\sigma_1}{\sigma_0-\sigma_1}\right) \\
\tilde{A}^s_{m0} &= \frac{\tilde{B}^s_{m0}}{a^{2m}}\left(\frac{\sigma_0+\sigma_1}{\sigma_0-\sigma_1}\right),
\end{aligned} \tag{24}$$

where

$$\begin{aligned}
A_{mn} &= \tilde{B}_{mn}\left(B+\frac{K_m(k_n a)}{I_m(k_n a)}\right) \\
a_{m0} &= \tilde{B}^c_{m0}\left(B_0+\frac{1}{a^{2m}}\right) \\
b_{m0} &= \tilde{B}^s_{m0}\left(B_0+\frac{1}{a^{2m}}\right).
\end{aligned} \tag{25}$$

Where the $\tilde{B}$s are:

$$\begin{aligned}
A_{00} &= \tilde{A}_{00} \\
\tilde{B}^c_{m0} &= \frac{I_{inj}}{\sigma_0 m\pi hb}\frac{\cos(m\phi_0)-\cos(m\phi_1)}{B_c b^{m-1}-b^{-m-1}} \\
\tilde{B}^s_{m0} &= \frac{I_{inj}}{\sigma_0 m\pi hb}\frac{(\sin(m\phi_0)-\sin(m\phi_1))\frac{\sin(m\phi_e)}{m\phi_e}}{B_c b^{m-1}-b^{-m-1}} \\
\tilde{B}_{0n} &= \frac{I_{inj}}{\sigma_0 m\pi hb}\frac{[(\cos(k_n z_0)-\cos(k_n z_1))]\frac{\sin(k_n z_e)}{k_n z_e}}{BI'_0\left(\frac{n\pi b}{h}\right)+K'_0\left(\frac{n\pi b}{h}\right)} \\
\tilde{B}^c_{mn} &= \frac{2I_{inj}}{\sigma_0 k_n \pi hb}\frac{[\cos(k_n z_0)\left(\cos(m\phi_0)\right)-\cos(k_n z_1)\cos(m\phi_0)]}{BI'_0\left(\frac{n\pi b}{h}\right)+K'_0\left(\frac{n\pi b}{h}\right)} \\
& \frac{\sin(m\phi_e)}{m\phi_e}\frac{\sin(k_n z_e)}{k_n z_e} \\
\tilde{B}^s_{mn} &= \frac{2I_{inj}}{\sigma_0 k_n \pi hb}\frac{[\cos(k_n z_0)\left(\sin(m\phi_0)\right)-\cos(k_n z_1)\sin(m\phi_0)]}{BI'_0\left(\frac{n\pi b}{h}\right)+K'_0\left(\frac{n\pi b}{h}\right)} \\
& \frac{\sin(m\phi_e)}{m\phi_e}\frac{\sin(k_n z_e)}{k_n z_e}.
\end{aligned} \tag{26}$$

APPENDIX

Spatial Integration of the US Perturbation The effect of an US perturbating the conductivity is calculated using the sensitivity:

$$dV_{meas} = \int r dr d\phi dz \delta(\sigma) Sens(r, \phi, z). \tag{1}$$

The order by order z integration can easy be solve analytically using they have the following integrals:

$$\begin{aligned} Z_1 &= \int_0^h \sin(k(z_t) \exp\left[-\left(\frac{z_t}{w_2}\right)^2\right] dz \\ &= -w_2 \frac{\sqrt{\pi}}{2} \exp\left[-\frac{(kw_2)^2}{4}\right] \\ &\text{Im}\left(erf\left[\frac{h_t}{w_2} + i\frac{kw_2}{2}\right] - erf\left[-\frac{ct}{w_2} + i\frac{kw_2}{2}\right]\right) \\ Z_2 &= \int_0^h \cos(kz_t) \exp\left[-\left(\frac{z_t}{w_2}\right)^2\right] dz \\ &= -w_2 \frac{\sqrt{\pi}}{2} \exp\left[-\frac{(kw_2)^2}{4}\right] \\ &\text{Re}\left(erf\left[\frac{h_t}{w_2} + i\frac{kw_2}{2}\right] - erf\left[-\frac{ct}{w_2} + i\frac{kw_2}{2}\right]\right) \end{aligned} \tag{2}$$

where $k(k_{n_M}, k_{n_I n})$, $z_t = z - ct$, $h_t = h - ct$, and erf is the error function. The $\rho\phi$ integrals are of the form:

$$\begin{aligned} R_1 = \int_0^b \int_0^{2\pi} & f(\phi) F(\rho; m_M, m_{In}, n_M, n_{In}) \\ & \exp\left[-\left(\frac{r_0^2}{w_1^2}\right)\right] \exp\left[\frac{2\rho}{w_1^2}(x_0 \cos(\phi) + y_0 \sin(\phi))\right] \\ & \exp\left[-\left(\frac{\rho}{w_1}\right)^2\right] d\phi d\rho, \end{aligned} \tag{3}$$

where the angular dependence is of the form

$$\begin{aligned} f(\phi; m_M, m_{In}) &= \cos(m_{In} + m_M) \pm \cos(m_{In} - m_M), \text{ or} \\ f(\phi; m_M, m_{In}) &= \sin(m_{In} + m_M) \pm \sin(m_{In} - m_M) \end{aligned}$$

For a radially symmetric US pulse, the orthogonality of $\cos(m\phi)$ and $\sin(m\phi)$ simply gives

$$\pi a_{mn_1} a_{mn_2} + \pi b_{mn_1} b_{mn_2} (2\pi a_{mn_1} a_{mn_2})$$

for $m > 0$ ($m = 0$). Moving the beam axis is off-center results in non-zero cross-terms $a_{m_1 n_1} b_{m_2 n_1}$ and mixes the different m-modes as the integration is of the form:

$$\begin{aligned} \int_0^{2\pi} & \exp\left[\frac{2\rho}{w_1^2}(r_0 \cos(\phi_0)\cos(\phi) + r_0 \sin(\phi_0)\sin(\phi))\right] \\ & \cos(m\phi) d\phi = 2\pi I_m\left(r_0 \frac{2\rho}{w_1^2}\right) \cos(m\phi_0) \\ \int_0^{2\pi} & \exp\left[\frac{2\rho}{w_1^2}(r_0 \cos(\phi_0)\sin(\phi) + r_0 \sin(\phi_0)\sin(\phi))\right] \\ & \sin(m\phi) d\phi = 2\pi I_m\left(r_0 \frac{2\rho}{w_1^2}\right) \sin(m\phi_0). \end{aligned} \tag{4}$$

The non-zero terms from the symmetric case become

$$\pi(\cos((m_1 + m_2)\phi_0) I_{m_1+m_2} \pm I_{m_1-m_2} \cos((m_1 - m_2)\phi_0))$$

for $a_{m_1 n_1}$, $a_{m_2 n_2}$ and $b_{m_1 n_1}$, $b_{m_2 n_2}$, respectively, while the cross terms become

$$\pi(\sin((m_1 + m_2)\phi_0) I_{m_1+m_2} + I_{m_1-m_2} \sin((m_1 - m_2)\phi_0))$$

for $b_{m_1 n_1}$ and $a_{m_2 n_2}$. The resulting ρ integral does not have a closed form. It can be useful to convolute the power series into a Cauchy product which reduces the ρ integral to the form:

$$\begin{aligned} R_1 &= \sum_{i=0}^{\infty} \int_0^b c_i x^{i+p} \exp\left[-\left(\frac{\rho}{w_1}\right)^2\right] d\rho \\ &= \sum_{i=0}^{\infty} c_n \frac{w_1^{i+p+1}}{2} \gamma\left(\frac{n+p+1}{2}, \left[\frac{b}{w_1}\right]^2\right), \end{aligned} \tag{5}$$

where $\gamma(n, x)$ is the lower incomplete gamma function.